# Atomically resolved magnetic structure of a Gd-Au surface alloy

Maciej Bazarnik, Mikel Abadia, Jens Brede, Michał Hermanowicz, Emil Sierda, Micha Elsebach, Torben Hänke, and Roland Wiesendanger

Phys. Rev. B **99**, 174419 — Published 21 May 2019

DOI: 10.1103/PhysRevB.99.174419

**Atomically resolved magnetic structure of a Gd-Au surface alloy**

Maciej Bazarnik[1,2], Mikel Abadia[3,4], Jens Brede[3,4], Michał Hermanowicz[2], Emil Sierda[1,2], Micha Elsebach[1], Torben Hänke[1], and Roland Wiesendanger[1]

[1] Department of Physics, University of Hamburg, Jungiusstrasse 11, D-20355, Hamburg, Germany.
[2] Institute of Physics, Poznan University of Technology, Piotrowo 3, 60-965 Poznań, Poland.
[3] Centro de Física de Materiales (Consejo Superior de Investigaciones Científicas (CSIC)/Universidad del País Vasco (UPV)-Euskal Herriko Unibertsitatea (EHU)-Materials Physics Center (MPC), Paseo Manuel Lardizabal 5, 20018 San Sebastián, Spain
[4] Donostia International Physics Center (DIPC), Paseo Manuel Lardizabal 4, 20018 San Sebastián, Spain

Abstract:

The magnetic structure of a monolayer thick $GdAu_2$ surface alloy on Au(111) has been investigated down to the atomic level by spin-polarized scanning tunneling microscopy. Spin-resolved tunneling spectroscopy combined with density functional theory calculations reveal the local spin polarization of both Gd and Au atomic sites within the surface alloy. Moreover, the impact of dislocation lines on the atomic-scale magnetic structure as well as on the local coercive field strength is demonstrated.

The need for steadily improved magnetic data storage devices drives the search for magnetic thin films with tailored properties. Among the binary alloys, combinations of two transition metals have been studied most widely, e.g., soft-magnetic Fe-Ni or hard-magnetic Co-Fe [1-2]. Combinations of transition metals with rare earth metals are also well known, e.g., Fe-Gd, Fe-Nd or Co-Tb alloy systems [2-4]. Fruthermore, combinations of transition metals with noble metals received considerable attention in the past, with Co-Pt and Fe-Pt as best examples [5]. Lately, a combination of rare earth elements with noble metals as ultra-thin films became of interest [6,7]. The corresponding bulk materials have been known for quite some time. In bulk, these alloys exhibit antiferromagnetic order [9]. However, as a surface alloy of 1ML thickness, both Gd-Au and Gd-Ag are ferromagnetic with an in-plane easy axis. Their Curie temperature differs substantially from 19K to 85K, depending on the choice of the noble metal element [7].

The structural, electronic and magnetic properties of ultrathin films can vary drastically depending on their thickness [2,10]. In multilayer systems, the magnetic properties can additionally be tuned by the interactions between different magnetic layers via non-magnetic spacer layers [11]. For monolayer (ML) magnetic films, substrate effects are particularly important and can have significant influences on their

structural, electronic and magnetic properties. This has already been demonstrated for ultrathin magnetic films grown epitaxially on monocrystalline metallic substrates which represent well-defined systems with a variety of magnetic properties ranging from ferromagnetic order with in-plane magnetic anisotropy, as observed for 1ML Fe grown on W(110) [12], to antiferromagnetic order with out-of-plane magnetic anisotropy, as found for 1ML Fe grown on W(001) [13], or very complex non-collinear magnetic states, such as the skyrmionic lattice of 1ML Fe grown of Ir(111) [14], or the Néel states of 1 ML Fe on Re(0001) [15].

The common problem of magnetic transition metal films is their high reactivity against impurities, i.e., hydrogen, oxygen, or carbon. One way of dealing with the sensitivity of surfaces of transition metal films to impurities is to cover them with graphene [16-20]. In practice, this is realized in opposite order by first growing a layer of graphene on an appropriate substrate, e.g., Ir(111), and subsequently intercalating the magnetic transition metal between the graphene and the metal substrate [16,17]. A variety of magnetic thin films intercalated in graphene-based systems has been studied, and exceptional magnetic properties, e.g., a magnetic hardening effect, have been found [17,18]. The growth procedure is, however, complicated, and it is easy to overheat the sample during intercalation leading to unwanted alloying of the transition metal with Ir [16,20]. Gd-Au and Gd-Ag surface alloys do not require any protective layer. The surface structure is robust and survives the coating with thin molecular films [21]. The relatively low temperature necessary to grow the surface alloy makes them experimentally accessible and thereby an essential class of surface-confined magnetic systems. In contrast to Fe- or Co-intercalated graphene, Gd-based surface alloys exhibit a significantly lower coercive field on the order of several mT. The moiré pattern found for those surface alloys can serve as a template for magnetic adsorbates [22,23]. Until now, little is known about the influence of local disorder, like atomic defects, dislocation lines, or rotational domains, on the electronic and magnetic properties of such surface alloys. In the following, we will address the magnetic structure of the $GdAu_2$ surface alloy grown on Au(111) with atomic resolution as well as the influence of structural defects on the local and spatially averaged magnetic properties.

Figure 1(a) shows an overview scanning tunneling microscope (STM) image of a single atomic layer thick $GdAu_2$ surface alloy film prepared on Au(111) according to an established procedure [6]. All our STM data have been obtained at a temperature of 6.5K. A moiré pattern with a periodicity of about 3.7 nm is visible. This moiré pattern arises due to the superposition of the $GdAu_2$ lattice and the underlying Au(111) lattice[6]. In addition, some irregularities caused by defects in the surface alloy film can be

observed. Three dislocation lines cross the area (marked with arrows in Figure 1(a)). Those lines separate two areas that are shifted with respect to each other by half a unit cell of the $GdAu_2$ lattice. A model of the alloy is overlaid on the topographies and is shown at the bottom of Figure 1. Choosing appropriate tunneling conditions one can easily observe the atomic structure of either Gd atoms or hexagons formed by Au atoms in constant-current STM data (Figure 1(b,c)). A model of the alloy is overlaid on both images. Differential tunneling conductance maps gathered at the same time at different bias voltages show the same surface area with energy-dependent sensitivity to either Gd or Au atomic sites (Figure 1(e,f)). Note that spatial variations in these maps are caused by the moiré pattern as well as by spatially dependent charge transfer. To understand the structure and determine the appropriate unit cell for our density functional theory calculations we investigated the moiré pattern in more detail. Several STM images with 50x50 $nm^2$ scan area and with atomic resolution were recorded. We took care to minimize the piezo creep and thermal drift for this particular data set. We then analyzed the 2D Fast Fourier transform (FFT) images. Correction of residual drift was performed by means of an affine transformation of 2D-FFT images. Figure 1(d) shows a raw data FFT map with a Bragg spot marked by a blue square and the moiré second beating spot marked by a red square. The full data set consisted of topography and corresponding differential tunneling conductance maps in which all six Bragg spots were very sharp. The exact positions of the moiré and Bragg spots in the FFT map were extracted by fitting 2D Gaussian peaks. The obtained coordinates were used to determine the length as well as the angle between the moiré and Bragg lattice vectors in reciprocal space. Finally, the angle was averaged over the six observed values giving a mean value of 30.8° with a standard deviation of 0.15°. The length of the reciprocal lattice vector of the first beating of the moiré is 0.145(7+-4)$a$. Where $a$ denotes the reciprocal lattice vector of the surface alloy. Using the Zeller approach [24,25] one can derive a simple relation:

$$\frac{a}{L} = \frac{r - \frac{s}{2}}{\cos(\theta)}$$

where $L$ is the reciprocal lattice vector of the moiré, $r$ and $s$ are the integer indices of the moiré unit cell and $\vartheta$ is the angle between the alloy's Bragg vector and the moiré vector. Using our data in the formula, we get r = 5.6 + s/2. Since r and s cannot be integers at the same time, the observed moiré is incommensurate.

Employing an antiferromagnetic Cr bulk STM-tip with in-plane sensitivity allows us to reveal the spatially resolved magnetic structure of the $GdAu_2$ surface alloy without disturbing influences of stray fields from the spin-sensitive probe tip. First, the Cr-tips were pre-characterized on known sample systems in order

to exclude tip-induced effects in the tunneling spectroscopy data. Subsequently, tunneling spectroscopy curves were recorded on the $GdAu_2$ surface alloy in external in-plane magnetic fields of +/-0.2 T (Figure 2(a)). This field value is sufficiently high to align the magnetization of the surface alloy film in two opposite directions. The normalization of the measured dI/dU signal over I/U allows us to directly compare with the LDOS of the calculated electronic structure. The spin asymmetry plot below the tunneling spectroscopy curve was computed according to:

$$\left(\frac{\frac{dI}{dU}}{\frac{I}{U}}\uparrow - \frac{\frac{dI}{dU}}{\frac{I}{U}}\downarrow\right)/\left(\frac{\frac{dI}{dU}}{\frac{I}{U}}\uparrow + \frac{\frac{dI}{dU}}{\frac{I}{U}}\downarrow\right)$$

and is a direct measure of the spin polarization of each state. The spectroscopy data presented in Figure 2(a) were obtained at the center of a protrusion within the moiré pattern marked by a blue dot in Figure 1(b). Spectroscopic data at other spots of the moiré differ with regard to the intensities of the observed features, but not their character (i.e. the electronic states contributing to those features) nor their spin polarization [26]. In the tunneling spectroscopy data, we observe occupied states which are barely spin-polarized. An unoccupied electronic state with a maximum at 0.6 V shows a slight spin asymmetry with a zero-crossing at the maximum of the spectroscopic feature, thereby pointing towards its spin-split nature. Furthermore, two pronounced spin-polarized unoccupied states at 2.5 V and 3.2 V appear. Here again, the spin asymmetry crosses zero close to the maximum of the spectroscopic feature. Note that the highest spin polarization is observed for unoccupied electronic states quite far from the Fermi level. In order to explain this experimental finding, we performed density functional theory (DFT) calculations.

We have used pseudopotential spin-polarized DFT as implemented in the SIESTA [27] code with generalized gradient approximation (GGA) within the Perdew-Burke-Ernzerhof (PBE) scheme for the exchange-correlation functional and double zeta basis set with polarization orbitals. We have calculated partial densities of states (PDOS) with 4x4x1 Monkhorst-Pack sampling of the surface Brillouin zone; the curves are extracted from the first surface ML only. The Fermi level (fixed at 0.0 eV in PDOS curves) has been fitted to match the Au *d*-states according to the ARPES data. Since the moiré in our samples is incommensurate, we used a relatively large unit cell ($(4,4)_{GdAu2}$ rot 34.5° on $(11,11)_{Au(111)}$) in our calculations in order to reproduce the experimental results as best as possible. Analyzing our DFT results as shown in Figure 2(b), we notice that the majority of the spin polarization of the system comes from the asymmetric occupancy of the Gd 4f-states. This then polarizes the Gd 5d-states as well as the Gd 6s-

states to some extent. The spin polarization of the Au electronic states is much smaller. Note that most of the spin polarization is found for the unoccupied states as observed in our experiments.

Before we assign the PDOS summed over all surface atoms as shown in Figure 2(b), to our experimentally observed spectroscopic features, we emphasize, that the Gd 4f states are highly localized and decay rapidly into the vacuum. Therefore, it is highly unlikely to directly observe these states with STM. Consequently, the spectroscopic features in the occupied state regime are assigned to mainly Au 6s-states, the feature at 0.6 V to a sum of Au 5d- and 6s-states (mainly due to their spatial localization at the Au atomic sites of the alloy), and finally the features at 2.5 V and 3.2 V to Gd 5d-states primarily. Note that the Gd 6s-states are spreading over the whole energy range with almost constant and rather small density. Not surprisingly, the magnetism of the $GdAu_2$ surface alloy originates from the split Gd 4f-states. However, we clearly observe in our experiments that both states derived from Gd as well as from Au are spin-polarized. To further support this claim we performed spatially resolved spin-polarized (SP-)STM measurements.

For each selected energy, a constant-current SP-STM image and a spin-resolved differential tunneling conductance map were recorded in opposing magnetic fields. Based on spatially and spin-resolved dI/dU data, the spin asymmetry maps were derived. Figure 2(c) shows two such spin asymmetry maps corresponding to the particular spin-resolved differential tunneling conductance maps presented in Figure 1(e,f). In both maps, a spin contrast of the same sign is visible. Since the selected energies are corresponding to the Au- and Gd-states, the presented spin asymmetry maps are in fact element-specific. From these maps, we can conclude that both elements exhibit spin-polarized states within the surface alloy. In fact, this is in line with an RKKY mechanism of interaction between Gd atoms via Au-derived states. The spatial variations in the spin-resolved differential tunneling conductance caused by the moiré pattern do not influence the sign of the measured spin asymmetry. The DFT calculations show that the Gd atoms carry a magnetic moment of nearly 8 $\mu_B$, while Au atoms have a moment of only 0.07 $\mu_B$. DFT also shows that the Au layer below the surface alloy is only marginally spin-polarized, i.e. four times less than the Au in the surface alloy layer. The orientation of the Au magnetic moments in the surface alloy layer is parallel with respect to the Gd magnetic moments.

To address the response of the surface alloy to the external magnetic field in more detail we performed large-scale SP-STM and spin-resolved differential tunneling conductance measurements as a function of external magnetic field strength. Figure 3(a) shows the SP-STM image of an extended area covering two terraces of the underlying Au(111) substrate. Figures 3(b) and (d) show spin-resolved differential

tunneling conductance maps recorded at identical tunneling parameters, but at different external magnetic fields. Note, that in our notation "+" and "–" signs of the external magnetic field refer to its inverted orientation. The direction of the in-plane magnetic field is parallel to the x-axis of the SP-STM images shown here. We observe a fully saturated magnetic contrast at -0.5 T. However, the maps show distinct lines showing electronic states at the dislocation lines. Moreover, there are two small areas of the bare Au(111) substrate present. When lowering the external magnetic field to around -10 mT, we observe the formation of magnetic domains. In the proximity of dislocation lines, a sharp change of magnetic contrast appears on opposing sides. In contrast to sample systems, where the direct magnetic exchange interaction is driving the ferromagnetism and defects in the structure do not affect the magnetization state, here dislocation lines appear to have a strong influence on the local magnetic structure of the film. If the magnetic domain is sufficiently large, the contrast gradually develops into the dominating dark blue indicating an antiparallel alignment of the tip and sample magnetization directions. In this case we observe the formation of a magnetic domain wall. At 0 T and in small positive fields we observe a mostly dark-bright-dark contrast of small domains influenced by the dislocation line structure. However, domain walls in larger domains remain unchanged. With increasing positive magnetic field we observe the propagation of domain walls and finally a reversion of the magnetization direction of the majority of the domains. At +50 mT only the smallest domains remain fully dark, while almost all dislocation lines remain decorated by narrow domains of dark contrast which rapidly diminish with increasing field strength. Finally, at +0.5 T the whole sample is fully saturated giving rise to a homogeneous bright contrast. In this data set we observe predominantly a two-level contrast with minor areas showing an intermediate contrast. In principle, for this six-fold symmetric surface alloy we would expect six degenerate in-plane magnetization directions and therefore also six levels of contrast in spin polarized differential tunneling conductance measurements. However, since this data set was gathered after fully saturating the film with an external magnetic field and the film shows remanence, therefore two directions of magnetization are prefered. Figure 3(c) shows the spatially averaged spin-resolved differential tunneling conductance signal from each measurement as a function of the external magnetic field. The obtained hysteretic loop reveals a coercive field of 17.5 mT. This is an order of magnitude larger than that reported by Ormaza et al [7]. This, in fact, shows how the local magnetic properties of the $GdAu_2$ surface alloy are affected by local defects that are causing enhanced coercive field strength of the otherwise rather soft magnetic alloy.

Finally, we would like to address the structure of dislocation lines in the surface alloy in more detail as their role for the local magnetic properties proved to be significant. Figure 4 shows a zoom-in SP-STM

image of such a defect together with simultaneously gathered spin-resolved differential conductance map at an energy of 3V showing predominantly the Gd sites with atomic resolution. There are only two directions under which the dislocation line extends, both of which are visible in the presented figure. Both are following the directions of lines connecting Gd-Gd nearest neighbors and are 60°-rotated with respect to each other. By matching the atomic structure of the surface alloy we extracted two possible models presented in panel (c) of figure 4. In both cases the distance between Gd atoms is changed with respect to the unperturbed lattice. In one case the distance between Gd atoms on opposite sides of the defect line is shortened, in the other case it is elongated. Moreover, the defect line allows for relaxation of the surface alloy which is evident as the fit of the atomic lattice to the SP-STM image is not perfect. Since DFT calculations at the appropriate level of accuracy for a unit cell being large enough to include a defect line are not feasible, we can only speculate on the physical explanation of the observed changes in the magnetic properties in the proximity of the defect line. One explanation is that the modified distance of Gd atoms changes the sign of the interaction in the RKKY coupling scheme. That would imply that the coupling strength is different for different directions of the dislocation lines. We did not observe that in our data. SP-STM studies in a fully rotatable in-plane magnetic field would be necessary in order to test that hypothesis. Alternatively, an edge state located on the defect line might possess a net magnetic moment and be responsible for the observed effects.

In summary, we presented atomically resolved spin-polarized STM data of a $GdAu_2$ surface alloy. We showed that both Gd and Au atoms are spin-polarized within the alloy and identified the most strongly polarized electronic states accessible by SP-STM as Gd 5d-states based on our DFT calculations combined with local spin-resolved tunneling spectroscopy data. Finally, we showed that dislocation lines have a significant influence on this two-dimensional surface alloy system causing a local enhancement of the coercive field strength.

Acknowledgments:
We gratefully acknowledge financial support from the Office of Naval Research via grant No. N00014-16-1-2900. Moreover, M.A. and J.B. acknowledge funding from the Spanish MINECO under contract Nos. MAT2013-46593-C6-4-P and MAT2016-78293-C6-5-R as well as the Basque Government Grants IT621-13 and IT-756-13, T.H. acknowledges support by the DFG under Grant No. HA 6037/2-1, E.S. acknowledges financing from Polish budget funds for science in 2014-2017 as a research project in the program "Diamond Grant" no. 0084/DIA/2014/43, M.H. acknowledges the support from by the Ministry of Science

and Higher Education in Poland within Project realized at Faculty of Technical Physics, Poznan University of Technology, and Poznan Supercomputing and Networking Center (PSNC).

References:

1. F. Pfeifer, C. Radeloff, J. Magn. Magn. Mater. **19**, 190-207 (1980)
2. B. Heinrich, J.A.C. Bland (Eds.), *Ultrathin Magnetic Structures*, Springer, Berlin (1994)
3. Yi Li, C. Polaczyk, F. Mezei, D. Riegel, Physica B: Cond. Matter **234-236**, 489-491 (1997)
4. T.M Danh, N.H Duc, N.P Thuy, J. Magn. Magn. Mater. **185**, 105-108 (1998)
5. M. Kitada, Thin Solid Films **146**, 21-26 (1987)
6. M. Corso, L. Fernández, F. Schiller and J.E. Ortega, ACS Nano, **4**, 1603–1611 (2010)
7. M. Ormaza, L. Fernández, M. Ilyn, A. Magaña, B. Xu, M.J. Verstraete, M. Gastaldo, M.A. Valbuena, P. Gargiani, A. Mugarza, A. Ayuela, L. Vitali, M. Blanco-Rey, F. Schiller, and J.E. Ortega, Nano Lett. **16**, 4230-4235 (2016)
8. T.R. McGuire and R.J. Gambino, J. App. Phys. **50**, 7653 (1979)
9.M. Gasgnier, Handbook on the Physics and Chemistry of Rare Earths **5**, 1-115 (1982)
10. H.H. Nalwa *Handbook of Thin Film Materials: Nanomaterials and Magnetic Thin Films*, Academic Press (2002)
11. Mark A. Howson, Contemporary Physics **35**, 347-359 (1994)
12. M. Bode, R. Pascal, and R. Wiesendanger, J. Vac. Sci. & Tech. A **15**, 1285 (1997)
13. A. Kubetzka, P. Ferriani, M. Bode, S. Heinze, G. Bihlmayer, K. von Bergmann, O. Pietzsch, S. Blügel, and R. Wiesendanger, Phys. Rev. Lett. **94**, 087204 (2005)
14. S. Heinze, K. von Bergmann, M. Menzel, J. Brede, A. Kubetzka, R. Wiesendanger, G. Bihlmayer, S. and Blügel, Nature Physics **7**, 713-718 (2011)
15. A. Palacio-Morales, A. Kubetzka, K. von Bergmann, and R. Wiesendanger, Nano Lett. **16**, 6252-6256 (2016)
16. M. Bazarnik, R. Decker, J. Brede, and R. Wiesendanger, Surf. Sci. **639**, 70 (2015)
17. R. Decker, J. Brede, N. Atodiresei, V. Caciuc, S. Blügel, and R. Wiesendanger, Phys. Rev. B **87**, 041403 (2013)
18. R. Decker, M. Bazarnik, N. Atodiresei, V. Caciuc, S. Blügel, and R. Wiesendanger, J. Phys.: Condens. Matter **26**, 394004 (2014)
19. M. Bazarnik, J. Brede, R. Decker, and R. Wiesendanger, ACS Nano **7**, 11341 (2013)
20. J. Brede, J. Sławińska, M. Abadia, C. Rogero, J.E. Ortega, I. Piquero-Zulaica, J. Lobo-Checa, A. Arnau and J.I. Cerdá, 2D Materials **4**, 015016 (2016)
21. M. Abadia, M. Ilyn, I. Piquero-Zulaica, P. Gargiani, C. Rogero, J.E. Ortega, and J. Brede ACS Nano **11**, 12392-12401 (2017)
22. M. Corso, L. Fernandez, F. Schiller, J.E. Ortega, ACS Nano **4**, 1603−1611 (2010).
23. H. Brune, M. Giovannini, K. Bromann, and K. Kern, Nature **394**, 451 (1998).
24. P. Zeller and S. Günther, New J. Phys. **16**, 083028 (2014)
25. P. Zeller X. Ma and S. Günther, New J. Phys. **19**, 013015 (2017)

26. See Supplemental Material at URL [Spin-polarized tunneling spectroscopy in external magnetic fields recorded at different spots of moiré pattern].
27. J.M. Soler, E. Artacho, J.D. Gale, A. García, J. Junquera, P. Ordejón and D. Sánchez-Portal, J. Phys. Cond. Matter **14**, 2745 (2002).

Figure 1:

(a) An overview STM image of a $GdAu_2$ surface alloy. Arrows mark dislocation lines. (b, c) Atomically resolved STM constant-current images and simultaneously measured differential tunneling conductance maps (e, f) at bias voltages of 3 V and 0.75 V corresponding to the energies of the Gd- and Au-derived electronic states, respectively. A model of the surface alloy is shown in both images as well as on the bottom: red corresponds to Gd sites, green for Au sites. A rhomb indicates atoms visible in (b) and (e) and a hexagon shows atoms visible in (c) and (f). A blue spot marks the position of spectra presented in Figure 2(a). (d) The 2D-FFT of a 50x50 $nm^2$ STM image. A Bragg spot and a $2^{nd}$ order moiré spot are marked. Isoheight lines of a 2D Gauss fit are shown in the inserts in (d).

Figure 2:

(a) Spin-polarized tunneling spectroscopy data obtained at the center of the protrusion within the moiré pattern. Below the corresponding spin asymmetry derived from the measured spin-resolved differential tunneling conductance curves is presented. (b) Calculated PDOS for different surface atoms and their electronic states. Each plot shows violet and green curves for the opposing spin channels and the corresponding spin asymmetry (filled blue). (c) Spin asymmetry maps for energies corresponding to the Gd- and Au-states, as derived from the measured spin-resolved differential tunneling conductance maps shown in Figure 1(e-f). A model of the surface alloy is overlaid on top of the maps.

Figure 3:

(a) SP-STM constant-current image of the $GdAu_2$ surface alloy with two Au(111) substrate steps. Uncovered Au(111) surface regions are visible at the top and lower left part of the image. (b) A spin-resolved differential tunneling conductance map recorded at -500 mT in-plane field. The signal is homogeneous except for dislocation lines and terrace edges showing additional electronic states. (c) Magnetic hysteresis curve as derived from the spin-resolved differential tunneling conductance signal spatially averaged over the whole area of the SP-STM measurement as a function of external magnetic field. (d) A series of spin-resolved differential tunneling conductance maps recorded as a function of in-plane magnetic field strength.

Figure 4:
(a) SP-STM image of a defect line in the $GdAu_2$ surface alloy. A model of the alloy is overlaid. (b) Spin-resolved differential tunneling conductance map recorded simultaneously with the constant-current image in (a). Same overlay is used in this panel. (c) Two types of defect lines with shorter and longer Gd-Gd nearest neighbor distances, respectively.

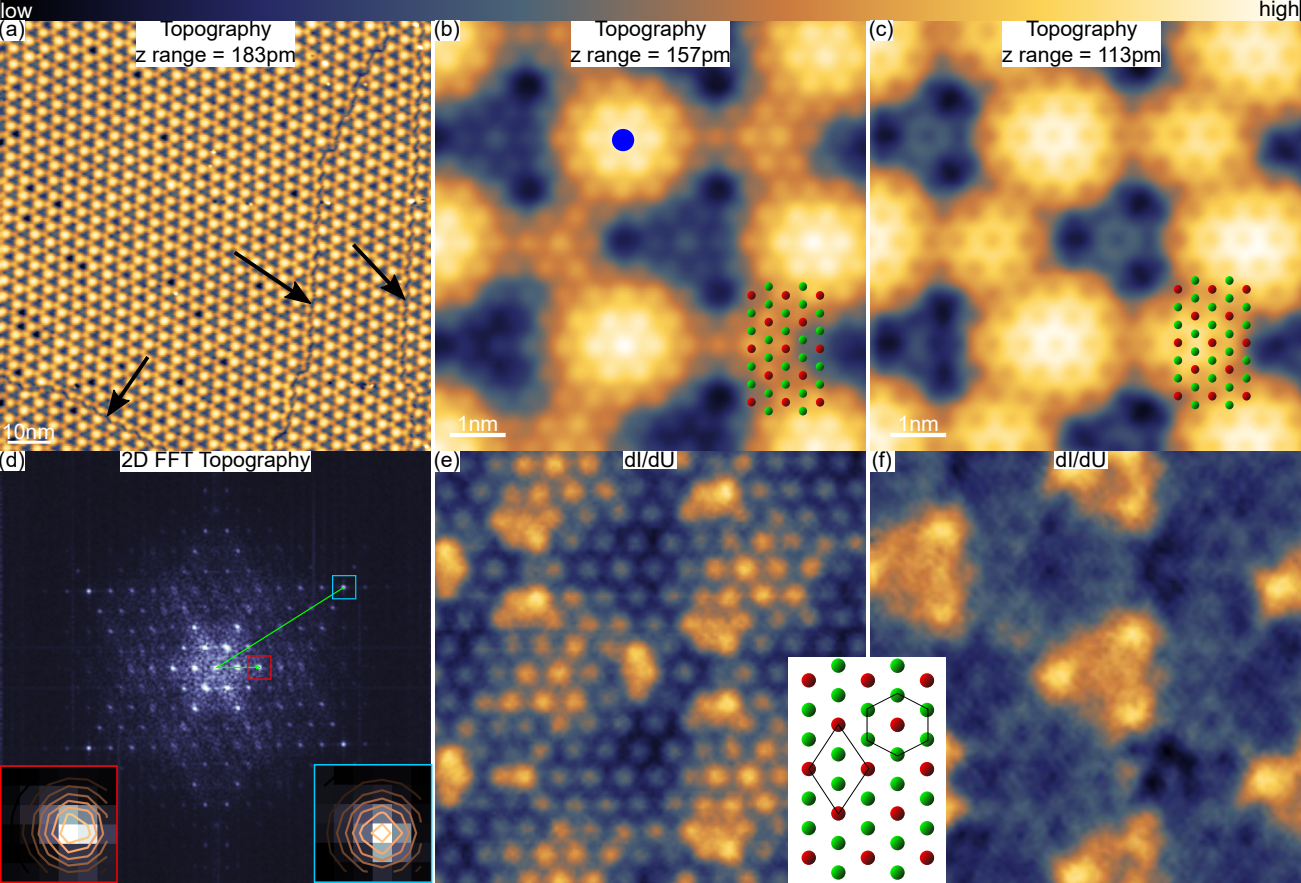
low
high
(a)
Topography
z range = 183pm
10nm
(b)
Topography
z range = 157pm
1nm
(c)
Topography
z range = 113pm
1nm
(d)
2D FFT Topography
(e)
dI/dU
(f)
dI/dU

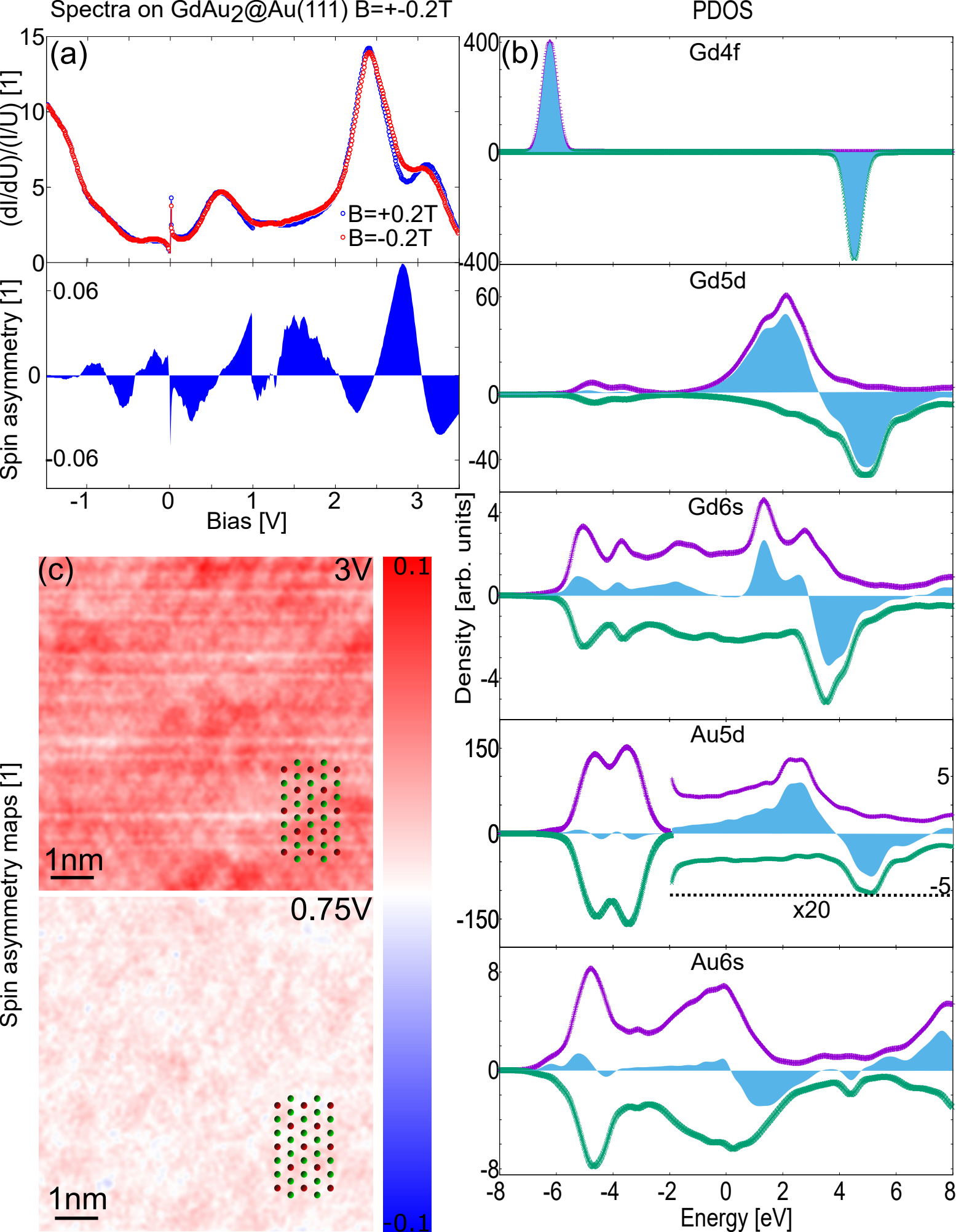
Spectra on GdAu2@Au(111) B=+-0.2T
PDOS
(a)
(dI/dU)/(I/U) [1]
B=+0.2T
B=-0.2T
Spin asymmetry [1]
0.06
-0.06
Bias [V]
(b)
Gd4f
Gd5d
Gd6s
Au5d
Au6s
Density [arb. units]
x20
Energy [eV]
(c)
3V
0.75V
1nm
Spin asymmetry maps [1]

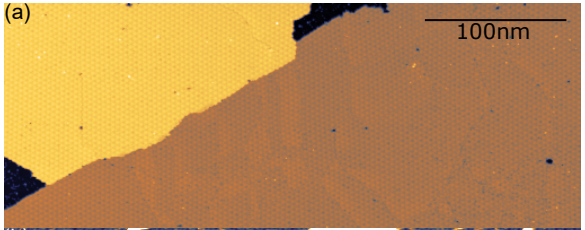
(a)
100nm

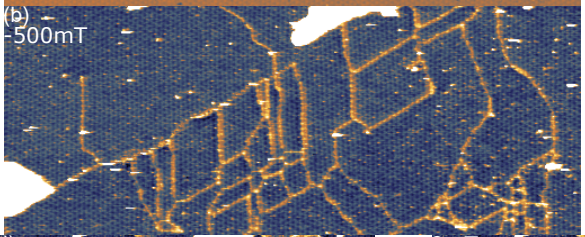
(b)
-500mT

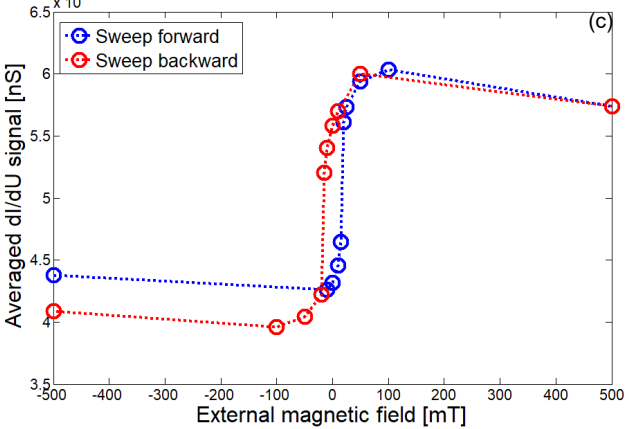
x 10^-10
(c)
Sweep forward
Sweep backward
Averaged dI/dU signal [nS]
External magnetic field [mT]
6.5
6
5.5
5
4.5
4
3.5
-500
-400
-300
-200
-100
0
100
200
300
400
500

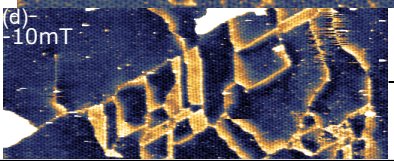
(d)
-10mT

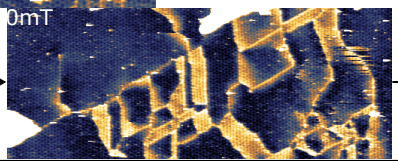
0mT

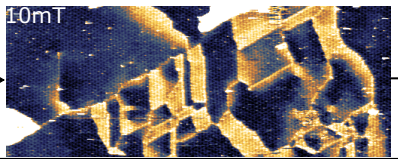
10mT

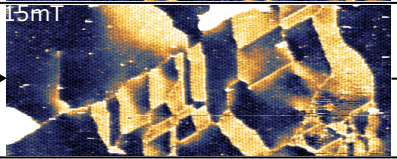
15mT

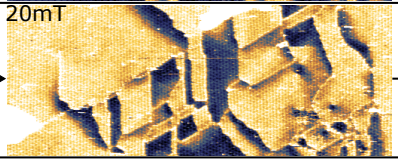
20mT

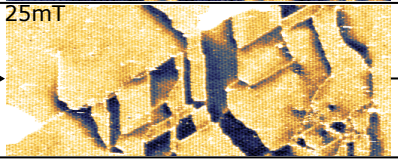
25mT

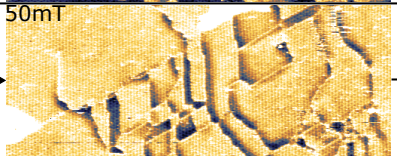
50mT

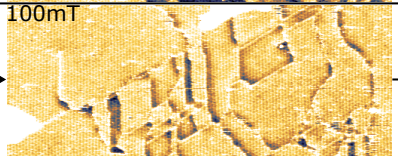
100mT

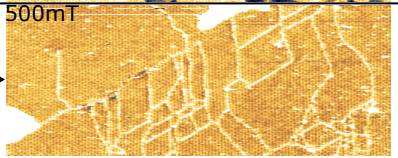
500mT

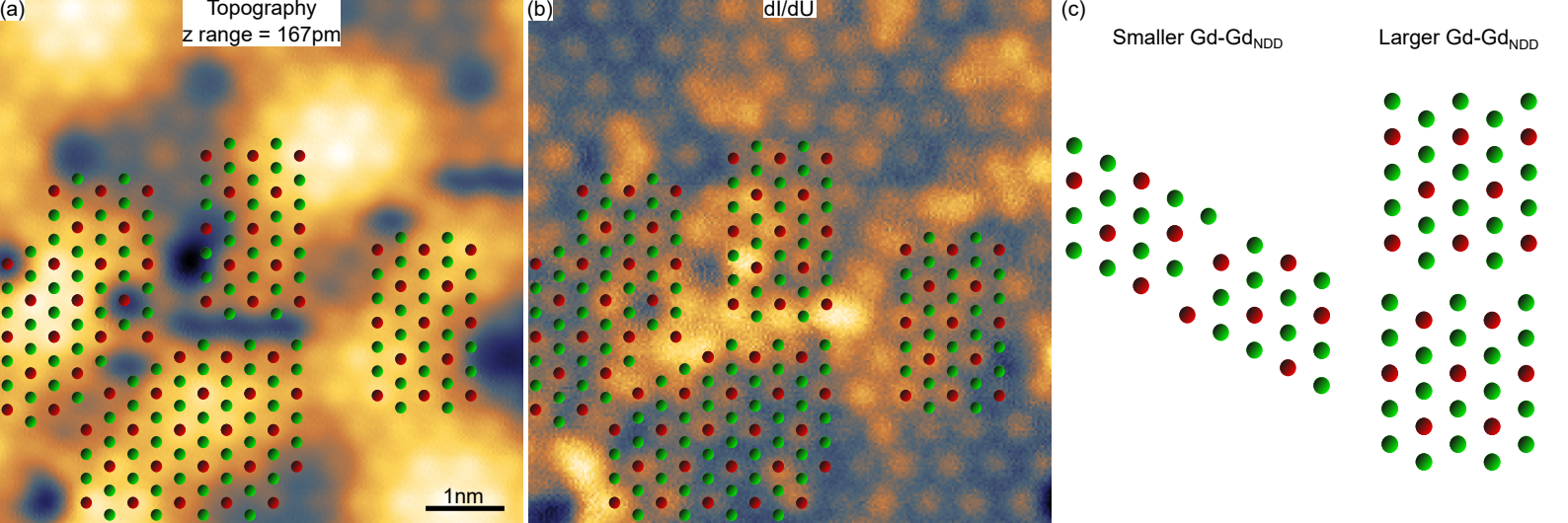
(a)
Topography
z range = 167pm
1nm
(b)
dI/dU
(c)
Smaller Gd-Gd$_{NDD}$
Larger Gd-Gd$_{NDD}$